Microscopy AND
Microanalysis

Original Article

Visibility and Apparent Size of Néel-Type Magnetic Skyrmions in Fresnel Defocus Images of Multilayer Films

Thibaud Denneulin[1]* , Jan Caron[1], Knut Müller-Caspary[1,2] , Olivier Boulle[3], András Kovács[1]
and Rafal E. Dunin-Borkowski[1]

[1]Ernst Ruska-Centre for Microscopy and Spectroscopy with Electrons and Peter Grünberg Institute, Forschungszentrum Jülich, 52425 Jülich, Germany; [2]Department of Chemistry, Ludwig-Maximilians-Universität München, Butenandtstrasse 5-13, 81377 Munich, Germany and [3]Université Grenoble Alpes, CNRS, CEA, Grenoble INP, Spintec, Grenoble, France

Abstract

Multilayers that comprise thin films of heavy metals and ferromagnets have been shown to host Néel-type magnetic skyrmions at room temperature. Fresnel defocus imaging in Lorentz transmission electron microscopy is a widely used technique for recording magnetic information about skyrmions. However, the visibility of Néel-type skyrmions in Fresnel defocus images is typically low, both because only a small component of their magnetic field contributes to the signal and because of the presence of diffraction contrast from the polycrystalline multilayer structure. Here, we take advantage of the out-of-plane hysteresis in such samples to record background-subtracted Fresnel defocus images. We demonstrate an improvement in magnetic signal-to-noise ratio and spatial resolution by a factor of 3 for a (Pt/Co/NiFe)×5 multilayer. We also use simulated Fresnel defocus images of Néel-type magnetic skyrmions to understand the influence of defocus on apparent skyrmion size.

Key words: ferromagnetism, Fresnel defocus imaging, Lorentz microscopy, multilayers, Néel-type magnetic skyrmions, transmission electron microscopy

(Received 4 June 2021; revised 20 August 2021; accepted 28 September 2021)

Introduction

Magnetic skyrmions are whirl-like spin textures, which are foreseen as elementary building blocks in future low-power storage and logic devices (Nagaosa & Tokura, 2013; Fert et al., 2017). Magnetic skyrmions were first observed at low temperature in bulk crystals of B20 compounds (Mühlbauer et al., 2009; Yu et al., 2010), as a result of the Dzyaloshinskii–Moriya interaction (DMI) (Dzyaloshinsky, 1958; Moriya, 1960). Subsequently, stacks of thin layers of heavy metals and ferromagnets with the DMI at their interfaces (Bogdanov & Rößler, 2001) have been shown to host magnetic skyrmions at room temperature (Jiang et al., 2015; Boulle et al., 2016; Moreau-Luchaire et al., 2016; Woo et al., 2016). Magnetic interactions in such stacks can be tuned by changing the compositions of the layers, thereby providing control over magnetic skyrmion size and density (Soumyanarayanan et al., 2017). High-density storage applications require small magnetic objects and magnetic skyrmions that are as small as 10 nm have been reported (Büttner et al., 2018; Caretta et al., 2018). Magnetic imaging techniques with high spatial resolution and sensitivity are, therefore, required to investigate small magnetic skyrmions.

Several different magnetic imaging techniques have been used to study multilayer samples, including scanning transmission X-ray microscopy (Moreau-Luchaire et al., 2016; Woo et al., 2016), polar magneto-optical Kerr effect (MOKE) microscopy (Jiang et al., 2017; Schott et al., 2017), magnetic force microscopy (Zhang et al., 2018c; Casiraghi et al., 2019), and Lorentz transmission electron microscopy (LTEM) (Pollard et al., 2017). Fresnel defocus imaging in LTEM is a widespread technique for investigating magnetic spin textures with high spatial resolution (Chapman, 1984; Phatak et al., 2016). When electrons pass through a magnetic induction field $B_\perp$ that is oriented perpendicular to their trajectory, they are deflected by the Lorentz force. To a first approximation, the deflection angle is given by the expression $\theta = (e\lambda/h) B_\perp t$, where e is the electron charge, λ is the electron wavelength, t is the specimen thickness, and h is Planck's constant. The deflection of the electron beam leads to variations in contrast at the locations of magnetic domain walls in Fresnel defocus images. However, in the case of an out-of-plane-magnetized layer that hosts Néel-type domain walls, there is no contrast at zero sample tilt angle (when the layer is perpendicular to the electron beam) because the curl of the magnetization has no component in the electron beam direction (McVitie & Cushley, 2006; Benitez et al., 2015). Contrast can be obtained by tilting the sample, so that a fraction of the out-of-plane magnetic field is projected onto a plane perpendicular to the optical axis of the microscope (Benitez et al., 2015; Pollard et al., 2017). Fresnel

CrossMark

defocus images have been used to study Néel-type magnetic skyrmions in a variety of multilayer samples (Pollard et al., 2017; He et al., 2018; McVitie et al., 2018; Fallon et al., 2019; Garlow et al., 2019; Jiang et al., 2019; Li et al., 2019) in the presence of different external stimuli (He et al., 2017; Zhang et al., 2018a, 2018b). However, it is difficult to obtain well-resolved Fresnel defocus images of small Néel-type magnetic skyrmions with high contrast for several reasons. First, as the constituent ferromagnetic layers are very thin (often only a few atomic layers in thickness), the magnetic signal integrated along the electron beam path is weak. It can be increased by repeating the layer stack to increase the total thickness of ferromagnetic material, but the repetition of heavy metal layers reduces the transmitted beam intensity. Second, the polycrystalline structure of layers that have been deposited by sputtering can create a rapidly varying background associated with diffraction contrast from individual grains, which is superimposed on the magnetic phase contrast. Third, the use of a large sample tilt angle to increase the magnetic contrast also increases the projected sample thickness, which reduces the transmitted intensity and results in weak contrast. Fourth, if the magnetic field of the conventional microscope objective lens is used to stabilize magnetic skyrmions, then the in-plane component of this field in a tilted sample can lead to deformations of the magnetic skyrmion texture (Zhang et al., 2020). As a result of these problems, it is often necessary to use large defocus values (typically several mm) to obtain sufficient magnetic contrast, which results in blurring and can lead to erroneous interpretation. Therefore, it is important to find strategies to improve the magnetic contrast and spatial resolution of Fresnel defocus images of Néel-type magnetic skyrmions.

Here, we investigate the benefits of using background subtraction to remove contributions from diffraction contrast on the quality of Fresnel defocus images of Néel-type magnetic skyrmions. We perform experiments on a ferromagnetically coupled (Pt/Co/NiFe)×5 multilayer and discuss the results in terms of magnetic signal-to-noise ratio (SNR) and spatial resolution. Defocus series of Fresnel images are also simulated based on theoretical skyrmion models, and the influence of defocus on apparent magnetic skyrmion size is assessed.

Materials and Methods

The sample studied here consists of a stack of nominal composition Ta(3)/Pt(1.5)/[Pt(1.5)/Co(0.3)/Py(0.9)]×5/Ru(0.5)/Pt(2), where the numbers between parentheses correspond to the thicknesses of the layers in nm, ×5 is the number of repetitions, and Py corresponds to permalloy ($Ni_{0.8}Fe_{0.2}$). In total, the stack contains 6 nm of ferromagnetic materials (Co and Py) and 14.5 nm of heavy metals (Pt, Ta, and Ru). The Pt/Co interfaces are expected to provide a large magnetic anisotropy perpendicular to the layers and host a large positive DMI. (Values of +1.5–+3 meV have been reported (Yang et al., 2015; Boulle et al., 2016; Jadaun et al., 2020).) On the other hand, the Pt/Py interface should host a negative DMI. (Values of approximately −1 meV have been reported for Pt/Py (Nembach et al., 2015) and Pt/Ni interfaces (Chen et al., 2013; Jadaun et al., 2020).) The stack was deposited directly onto a 15-nm-thick SiN membrane using DC magnetron sputtering. An image of a cross-section of the stack and corresponding compositional profiles are shown in Supplementary Information 1.

A magnetic hysteresis loop of the sample was recorded using a MOKE microscope in the presence of an out-of-plane external field.

Fresnel defocus imaging was carried out at room temperature using an FEI Titan TEM equipped with a Schottky field emission gun, a CEOS image aberration corrector, a C-TWIN objective lens with a large pole piece gap of 11 mm, and a 4k×4k Gatan K2-IS direct electron detector. The microscope was operated at 300 kV in magnetic-field-free conditions (Lorentz mode) by using the first transfer lens of the aberration corrector as the primary imaging lens. The conventional microscope objective lens was then used to apply chosen magnetic fields to the sample. The applied magnetic fields were pre-calibrated using a Hall probe. All of the applied magnetic field values referred to below correspond to fields in the electron beam direction (i.e., perpendicular to the sample when the stage is at 0°). Fresnel defocus series were recorded by changing the excitation of the transfer lens. Defocus values were calibrated by analyzing the spacing of Fresnel fringes produced at an opaque edge (Reimer & Kohl, 2008). Images were processed using Digital Micrograph (Gatan) software. Bright-field TEM imaging was carried out using the same microscope operated in conventional TEM mode with a small objective aperture centered around the transmitted beam.

Magnetization models of Néel-type skyrmions were calculated using an analytical expression described in Appendix A. These models were used as input to simulations of Fresnel defocus images, as described in Appendix B.

Results

Magnetic and Crystalline Structure of the Sample

Figure 1a shows Fresnel defocus images of the sample recorded at a defocus of −7.5 mm and a nominal sample tilt angle of 30° for different values of magnetic field applied using the conventional microscope objective lens. In zero applied magnetic field, the Fresnel defocus image shows black and white curved lines, which result from the presence of magnetic domains separated by domain walls. These magnetic domain walls produce very weak Fresnel defocus contrast at zero sample tilt (see Supplementary Information 2), suggesting that they are 180° Néel-textured walls (Benitez et al., 2015). In the presence of an applied magnetic field, the magnetic domain walls move and form black/white pairs (see the image at 23 mT), which are equivalent to 360° magnetic domain walls (Kubetzka et al., 2003). On increasing the applied magnetic field further, the magnetic domains are erased progressively. The image recorded at 46 mT corresponds to a saturated state with no magnetic contrast, as all of the magnetic moments in the sample are then close to being parallel and oriented out-of-plane.

In this first series of images, the number of magnetic skyrmions is low. To obtain more magnetic skyrmions, the sample was saturated in an in-plane direction, as reported in previous studies (Qin et al., 2018; Li et al., 2020). The in-plane magnetic field was applied in situ in the TEM by tilting the sample to 80° and exciting the conventional microscope objective lens fully (corresponding to an applied magnetic field of approximately 1.4 T) for a few seconds. The sample was then tilted back to 30° to record Fresnel defocus images, as shown in Figure 1b. A compact array of magnetic skyrmions of different size is now visible in zero applied magnetic field. A small perpendicular field was then applied again to decrease the density of the magnetic skyrmions and to stabilize them (see images at 23 and 37 mT).

Figure 1c shows a magnified image of an individual Néel-type magnetic skyrmion. The low and high spatial frequency
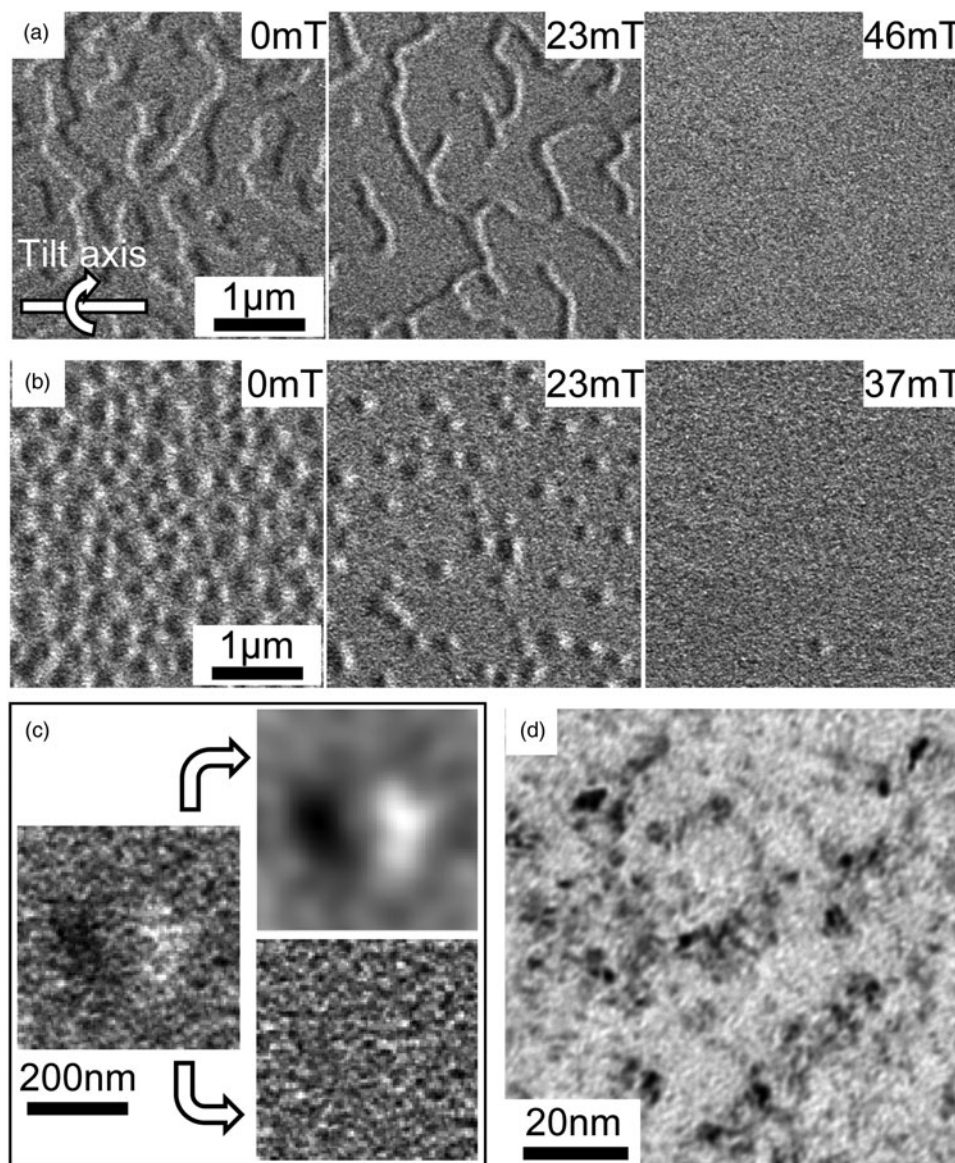
Fig. 1. (**a**) Fresnel defocus images of the (Pt/Co/NiFe)×5 multilayer film recorded in Lorentz mode using a defocus of −7.5 mm and a sample tilt angle of 30° in the presence of the indicated magnetic fields applied using the conventional microscope objective lens. (**b**) Fresnel defocus images recorded after in-plane magnetic saturation of the sample in the presence of the indicated magnetic fields. (**c**) *Left*: Magnified image of a single skyrmion; *Upper right*: low spatial frequency components of the image; *Lower right*: high spatial frequency components of the image. The low and high spatial frequency components were separated using a binary circular filter of radius $10\,\mu m^{-1}$ in Fourier space. (**d**) In-focus bright-field TEM image recorded at high magnification showing the polycrystalline grain structure of the sample.

components of the image, which were separated by using a band-pass filter of radius $10\,\mu m^{-1}$ applied in Fourier space, are shown in the upper right and lower right parts of Figure 1c, respectively. The low spatial frequency components, which take the form of a pair of black and white streaks aligned parallel to the tilt axis, are related to the out-of-plane skyrmion magnetization projected onto the image plane. The high spatial frequency components show an apparently random distribution of mottled contrast. This background degrades the visibility of the magnetic signal in the original Fresnel defocus image strongly. It originates primarily from diffraction contrast from individual small grains in the polycrystalline structure of the stack. Figure 1d shows crystal grains that have a size of approximately 5–10 nm in an in-focus bright-field TEM image. The separation of the magnetic signal

from diffraction contrast using Fourier filters would be reasonable for magnetic skyrmions that are significantly larger than the crystal grains. However, the use of Fourier filtering can degrade the spatial resolution of the image further and introduce additional artifacts, thereby preventing the observation of small magnetic skyrmions. Careful background subtraction is required to remove this mottled contrast without reducing the spatial resolution of the image appreciably.

Subtraction of the Non-magnetic Background

One possible approach for subtracting the non-magnetic background is to increase the applied magnetic field to saturate the magnetic moments in the sample and to record and subtract
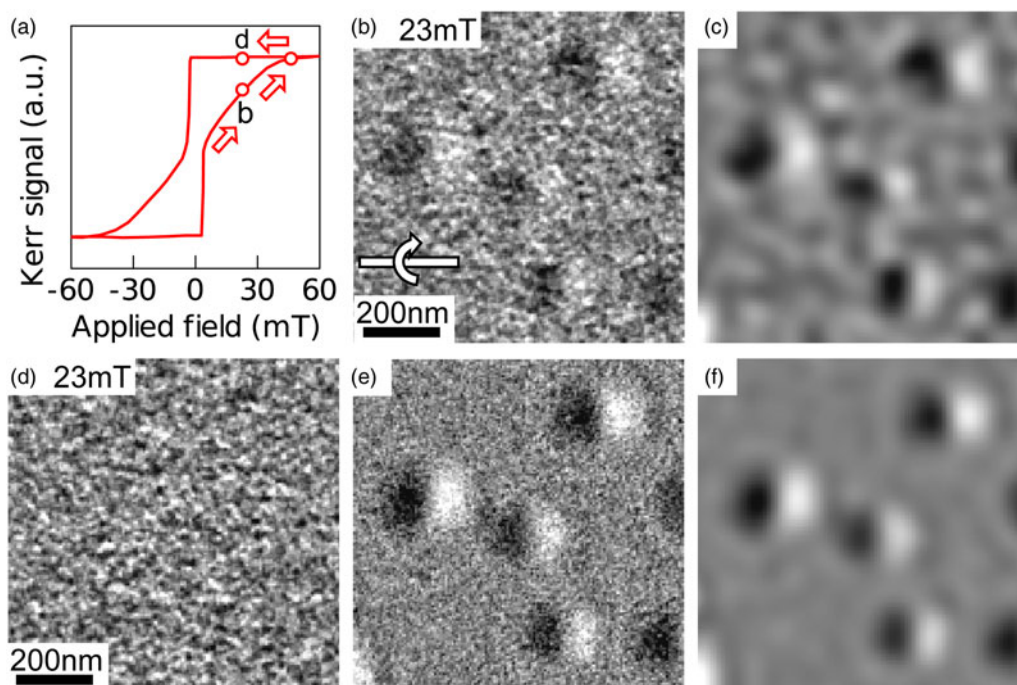
Fig. 2. (**a**) Magnetic hysteresis loop recorded using MOKE microscopy in the presence of an out-of-plane external field. (**b**) Fresnel defocus image of four magnetic skyrmions recorded in Lorentz mode at a defocus of −7.5 mm and a sample tilt angle of 30° in the presence of an applied magnetic field of 23 mT. The image is labelled "**b**" on the hysteresis curve. (**c**) Same image after the application of a low-pass filter of radius 10 μm^{-1} in Fourier space. (**d**) Fresnel defocus image recorded after increasing the applied magnetic field to achieve a saturated magnetic state (46 mT) and then decreasing it to the initial value of 23 mT. The image is labelled "**d**" on the hysteresis curve. (**e**) Difference between images (**b**) and (**d**) after alignment using cross-correlation. (**f**) Same image after the application of a low-pass filter of radius 10 μm^{-1} in Fourier space.

the corresponding image (see, for example, Park et al., 2020). However, this approach requires the alignment of the resulting images, taking into account changes in rotation and magnification due to the different excitation of the objective lens (see Supplementary Information 3). For small changes in the excitation of the objective lens, these problems can be circumvented by using the following approach. Figure 2a shows a magnetic hysteresis curve recorded from the sample using MOKE microscopy in an out-of-plane magnetic field. As shown in the previous section, individual magnetic skyrmions can be stabilized by applying a magnetic field of 23 mT (label 'b' on the hysteresis curve). Figure 2b shows a Fresnel defocus image of four magnetic skyrmions recorded at this field, and Figure 2c shows the same image after the application of a low-pass filter (of radius 10 μm^{-1} in Fourier space). The applied magnetic field was increased further to saturate the sample (at 46 mT) and then decreased to the initial field of 23 mT (label 'd' on the hysteresis curve). When the applied magnetic field was decreased after saturating the sample, the presence of a large plateau in the upper part of the hysteresis curve (between −5 and 45 mT) suggests that the sample should remain saturated, even at remanence, i.e., with the applied magnetic field removed. Figure 2d indeed shows that the corresponding Fresnel defocus image recorded at 23 mT contains mottled background contrast and no magnetic features. The rotation and magnification of the two images (b and d) are the same, making their alignment and subtraction more straightforward. For alignment, a simple shift of the images was applied using cross-correlation, in order to compensate for sample and/or image drift. (A simple alignment script for Digital Micrograph is provided in Supplementary Information 4). Figure 2e shows the difference between the two images, in

which the visibility of the magnetic skyrmions is improved significantly compared to (b). After the application of a low-pass filter, as shown in Figure 2f, the background is more uniform than in (c). It shows that the subtraction removes unwanted low frequency signals that the filter lets through. This subtraction procedure can be reproduced for different values of applied magnetic field. A series of background-subtracted images of different magnetic skyrmion densities is shown in Supplementary Information 5.

Defocus Series and SNR

In a Fresnel defocus image, in general the larger the defocus the stronger the magnetic contrast but the poorer the spatial resolution. To determine the smallest defocus value that can be used, images of individual Néel-type magnetic skyrmions were recorded over a defocus range of −6 mm to −375 μm, as shown in Figure 3a. Figure 3b shows the same series of images after background subtraction using the approach described in the previous section. In the original images, many of the skyrmions are barely visible as a result of the presence of the mottled diffraction contrast, in particular when the defocus is smaller than −3 mm. After background subtraction, magnetic skyrmions are visible over almost the entire range of defocus values. At the larger defocus values (−6 to −3 mm), most of the magnetic skyrmions look like dumbbells, with characteristic black and white contrast regions. At lower defocus values (smaller than −1.5 mm), the contours of the magnetic skyrmions become sharper, with the largest magnetic skymions showing a region of uniform contrast at their centers (see, for example, the magnetic skyrmion indicated by a white arrow in Fig. 3b at −1.1 mm defocus). The shapes of these objects agree with the definition of a magnetic bubble,
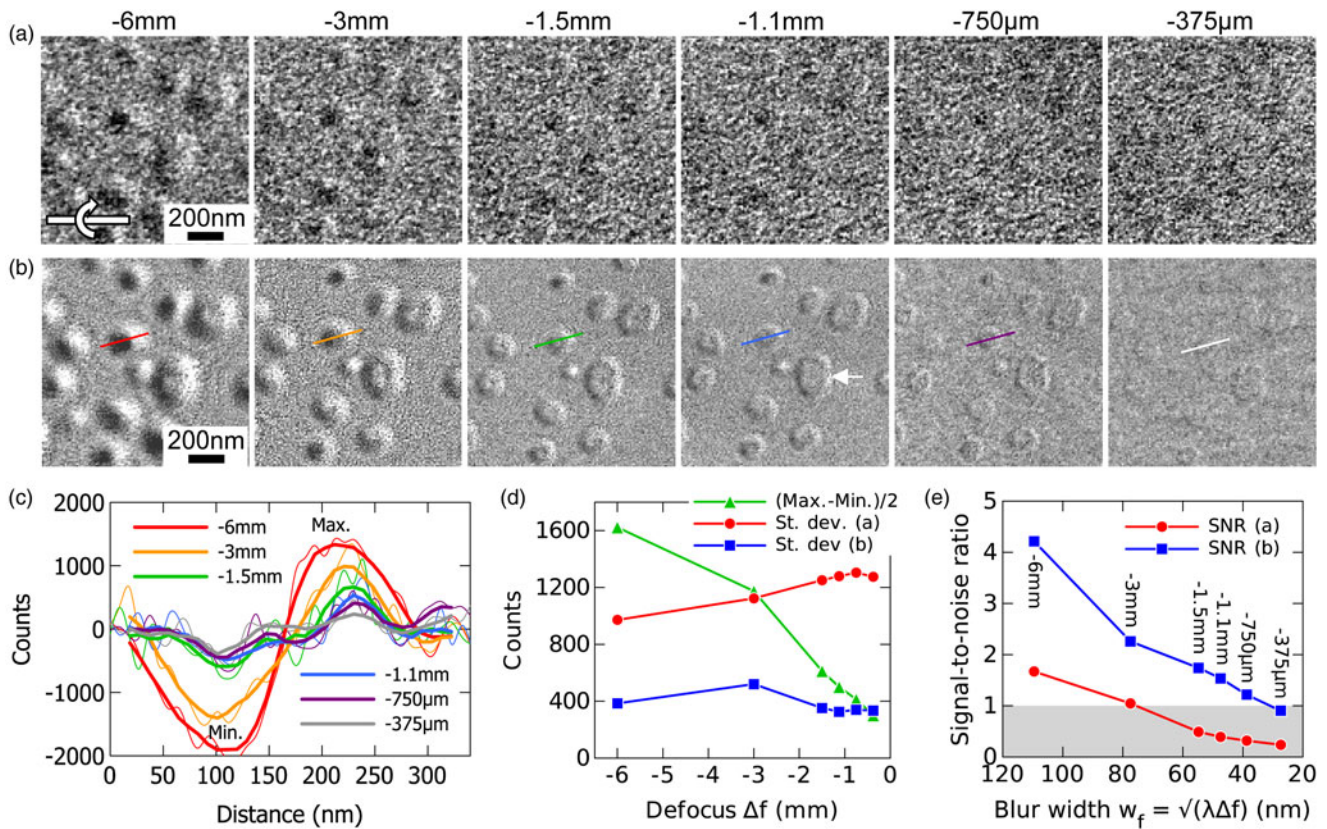
Fig. 3. (**a,b**) Fresnel defocus series of images recorded in Lorentz mode between −6 mm and −375 μm. The images are shown (**a**) before and (**b**) after subtracting the non-magnetic background. The sample tilt angle, applied magnetic field, and exposure time are 20°, 23 mT, and 8 s, respectively. (**c**) Intensity profiles across a magnetic skyrmion extracted along the lines marked in (**b**). Thin lines correspond to the raw data, while thick lines correspond to a moving average (averaged over 20 nm). The y axis shows both positive and negative values as a result of background subtraction. (**d**) Plots of the Max-to-Min intensity variations measured from (**c**) divided by 2 and the standard deviation of the background noise in (**a,b**) as a function of defocus. The standard deviation was calculated in a small region that contains no skyrmions. (**e**) The SNR calculated from the values in (**d**), plotted as a function of the width of the blur induced by the defocus (defined as the width of the first Fresnel fringe $w_f \approx \sqrt{(\lambda \Delta f)}$, where λ is the electron wavelength and Δf is the defocus). The defocus values are indicated with vertical labels. The gray region corresponds to the area where the visibility of the skyrmions is too low (SNR < 1).

which consists of a uniformly magnetized magnetic domain bounded by a narrow circular magnetic domain wall. It is known that multilayer samples can host different topological solitons, including magnetic bubbles and classic magnetic skyrmions (comprising a round magnetic domain wall surrounding a single out-of-plane spin) (Bernand-Mantel et al., 2018). For simplicity, the term magnetic skyrmion is used throughout this article to refer to all of these objects.

A quantitative description of the magnetic SNR in Fresnel defocus images of Néel-type magnetic skyrmions is now discussed. Figure 3c shows intensity profiles extracted across an individual magnetic skyrmion at different defocus values along the lines marked in Figure 3b. The amplitude of the magnetic signal in each profile was estimated by measuring the extrema in intensity at the dip and the peak (marked *Min.* and *Max.*). The average value is plotted in Figure 3d (green triangles). The background noise, which was estimated by calculating the standard deviation of the image in a small region that contained no skyrmions, is also plotted in Figure 3d for the two series of images (red circles for the images in (a) and blue squares for the images in (b)). Background subtraction is found to decrease the noise by a factor of 2–4, depending on the defocus value. On average, the improvement is a factor of 3.3 for the defocus values considered here. Figure 3e shows the SNR calculated from the values in Figure 3d and plotted as a function of the width of the blur

associated with the use of a finite value of defocus (defined as the width of the first Fresnel fringe $w_f \approx \sqrt{(\lambda \Delta f)}$, where λ is the electron wavelength and Δf is the defocus). The width of the blur provides an estimate of the spatial resolution in the images. The corresponding defocus values are marked using vertical labels on the plot. By definition, the visibility of the magnetic domain walls is too low when the SNR is below 1. In the original images, the SNR is equal to 1 for a blur width of 77 nm (corresponding to a defocus of −3 mm). After background subtraction, the SNR is equal to 1 for a blur width of 27 nm (corresponding to a defocus of −375 μm), giving an improvement factor of 2.8. We have also tried to improve the SNR in background-subtracted images by increasing the exposure time, which was 8 s for the images in Figure 3, but no further improvement could be obtained with longer exposures or cumulative acquisition. For the exposure time used here, the SNR is, therefore, not limited by shot noise caused by a low number of counts, but by residual non-magnetic information, which was not completely removed.

Apparent Size of Small Skyrmions

As described in the previous section, background subtraction provides improved magnetic contrast at smaller defocus values with better spatial resolution. In this section, optimized conditions are used to observe and measure the apparent sizes of small
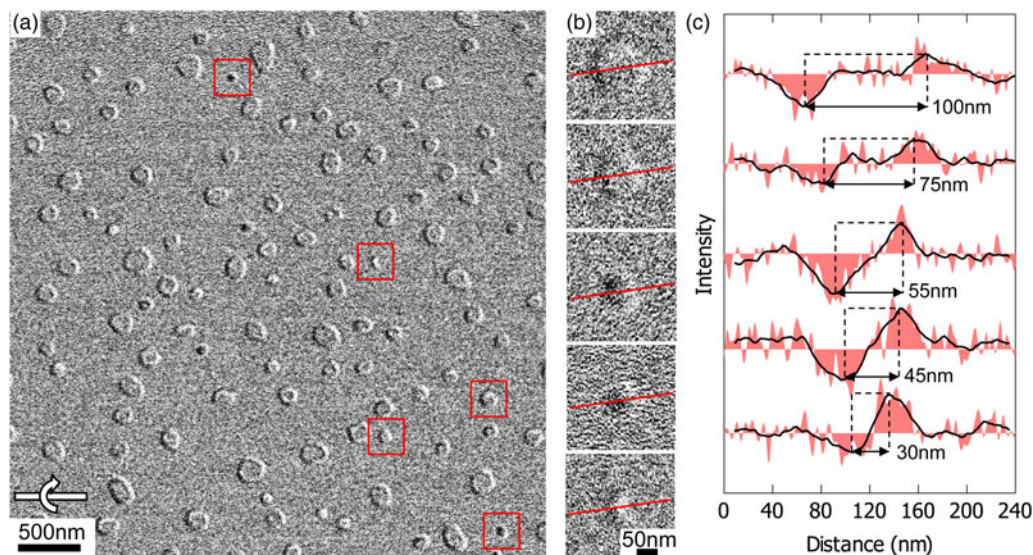
Fig. 4. (**a**) Background-subtracted Fresnel defocus image recorded at a defocus of −750 µm and a sample tilt angle of 20° in the presence of an applied magnetic field of 26 mT. (**b**) Magnified images of magnetic skyrmions of different size extracted from (**a**) at the positions marked by red squares. (**c**) Intensity profiles extracted from the images shown in (**b**) along the red lines. The filled curves correspond to raw data, while the black curves correspond to moving averages (averaged over 20 nm). The apparent size of each magnetic skyrmion, i.e., the distance between the dip and peak, is indicated on the plots.

magnetic skyrmions. The results are compared with simulated Fresnel defocus images. Figure 4a shows a background-subtracted Fresnel defocus image recorded with a large field of view using a relatively low defocus value of −750 µm, which corresponds to a blur width of approximately 40 nm. The image shows a large number of Néel-type skyrmions with different sizes, shapes, and contrasts. These variations can be related to the polycrystalline structure of the stack, which contains small and irregular grains. Magnetic textures can be influenced by grain boundaries, crystalline defects, local lattice deformations, and other non-uniformities of the stack. In addition, for small skyrmions that are not clearly resolved, Fresnel fringes from the two sides of the skyrmions overlap, which can also lead to complex variations of contrast. Magnified images and intensity profiles are shown in Figures 4b and 4c for a few selected magnetic skyrmions. The *apparent* size of each skyrmion is defined as the distance between the dip and the peak and is indicated on the plot in Figure 4c. The apparent sizes of the selected skyrmions vary between 100 and 30 nm. For skyrmions that are larger than 55 nm, the dip and the peak are well separated, and a core region of uniform intensity is visible. For skyrmions that are smaller than 55 nm, the dip and the peak overlap and the core region are no longer visible.

To understand how the blur resulting from the use of a finite defocus value influences the apparent size of the magnetic skyrmions, simulations of Fresnel defocus images of Néel-type magnetic skyrmions were performed. Figure 5a shows the magnetization field of a 50 nm Néel-type magnetic skyrmion calculated using the analytical expression given in the Appendix and observed at a sample tilt angle of 20° (with the tilt axis horizontal). The yellow curve shows the out-of-plane component of the magnetization field projected in the image plane in the horizontal radial direction. The skyrmion can be divided into three different regions, which include the outer and inner domains (where the out-of-plane magnetization is uniform and antiparallel) and the domain wall (where the magnetization varies). The *effective* magnetic skyrmion size (or skyrmion diameter) is defined as the diameter of the circle where the out-of-plane magnetization is zero.

Figure 5b shows a series of Fresnel images simulated for a defocus range of 100 µm to 3 mm. The curves plotted on the images show the corresponding intensity distributions in the radial direction parallel to the tilt axis (i.e., the horizontal direction in the image). For small defocus Δf, the intensity at a position $\mathbf{r}$ in a Fresnel image is given by the expression $I(\mathbf{r}, \Delta f) = 1 - \Delta f (e\mu_0 \lambda t/h)(\nabla \times \mathbf{M}(\mathbf{r})) \cdot \hat{\mathbf{z}}$ where e is the electron charge, μ_0 the vacuum permeability, λ the wavelength, t the specimen thickness, h Planck's constant, and $(\nabla \times \mathbf{M}(\mathbf{r})) \cdot \hat{\mathbf{z}}$ the component of the magnetization curl along the electron beam direction (McVitie & Cushley, 2006). For a Néel-type skyrmion at zero sample tilt angle, the z component of the magnetization curl is uniformly zero as the curl lies completely in the sample plane (Benitez et al., 2015; Pollard et al., 2017). When the sample is tilted with respect to the electron beam direction, the projection of the out-of-plane components of the magnetic field onto the observation plane leads to positive and negative variations of the z curl component on the opposite sides of the skyrmion along the tilt axis. Tilted in-plane components have a very weak contribution compared to the out-of-plane components (Jiang et al., 2019). Therefore, Fresnel defocus images show essentially a peak and a dip in intensity aligned along the tilt axis. For each image in Figure 5b, the *apparent* magnetic skyrmion size (i.e., the distance between the dip and the peak) was measured, as indicated on the images. At a low defocus value (100 µm), the apparent size matches the effective size of the magnetic skyrmion (50 nm). At intermediate defocus values (e.g. 700 µm and 1 mm), the size is underestimated (36 and 42 nm, respectively), as the Fresnel fringes from opposites sides of the magnetic skyrmion overlap and the uniform core region is no longer visible. At larger defocus values (2 and 3 mm), the size is overestimated (66 and 84 nm, respectively), with the overestimate increasing with defocus as the extent of the blur increases. Figure 5c shows the ratio between the apparent and effective skyrmion sizes plotted as a function of defocus for different effective skyrmion sizes. If the ratio is below 1, then the skyrmion size is underestimated. If it is greater than 1, then the skyrmion size is overestimated. The
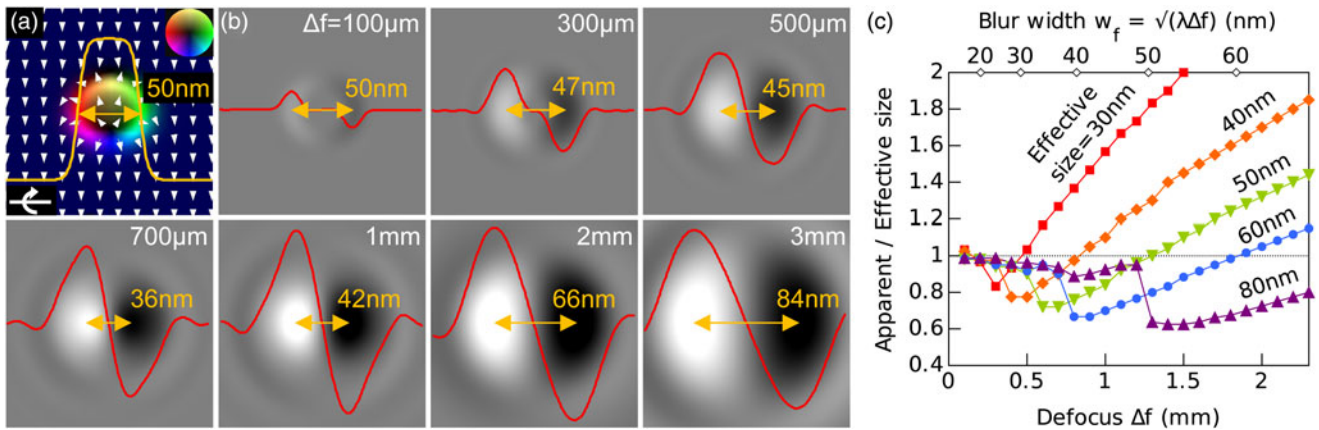
Fig. 5. (**a**) Theoretical magnetization distribution of a 50 nm Néel-type magnetic skyrmion for a sample tilt angle of 20° (with the tilt axis horizontal). The direction of the magnetization projected in the image plane is given by the colour wheel in the upper right corner and by the white arrows. The yellow curve corresponds to the out-of-plane component of the magnetization projected in the image plane in the horizontal radial direction. (**b**) Simulated Fresnel defocus images calculated from the model shown in (**a**) for the different defocus values indicated in the images. The red curves correspond to intensity profiles in the horizontal radial direction. The apparent size, i.e., the distance between the peak and the dip, is indicated on each image. (**c**) The ratio between the apparent size and the effective size of the magnetic skyrmion plotted as a function of defocus for magnetic skyrmions of different effective size. The upper x axis indicates the width of the first Fresnel fringe $w_f \approx \sqrt{(\lambda \Delta f)}$.

width of the first Fresnel fringe ($w_f \approx \sqrt{(\lambda \Delta f)}$) is indicated on the upper x axis of the plot. At lower defocus values, the ratio of apparent to effective size remains close to 1, so long as w_f is smaller than the effective skyrmion radius. On increasing the defocus, the ratio drops to 0.8–0.6, depending on the effective skyrmion size, when w_f is between the effective radius and the diameter of the skyrmion. For example, in the case of a 50 nm skyrmion (green triangles), the ratio shows a minimum at a defocus value of 600 μm, which corresponds to $w_f = 34$ nm. Beyond this minimum, the ratio increases with defocus and the slope is steeper for smaller skyrmions. The ratio becomes larger than 1 when w_f is larger than the effective skyrmion size.

The results show that different deviations in the apparent magnetic skyrmion size can occur depending on the defocus value, making it difficult to determine the true size of a small magnetic skyrmion that is not well resolved. For instance, in Figure 4, the apparent size of the smallest magnetic skyrmion is measured to be 30 nm. However, it may have a true size of approximately 50 nm if its size is underestimated at this defocus value. In the defocus series shown in Figure 3c, the skyrmion is larger and its apparent size is measured to be 130 nm at low defocus (see, for instance, the purple profile at −750 μm). By extrapolating the results of the simulations, the Fresnel fringes should overlap and the apparent skyrmion size should decrease when the value of w_f is between 65 and 130 nm, which corresponds to defocus values of approximately 2–8 mm. Indeed, the inner domain is not visible in the profiles obtained at −3 and −6 mm, and the apparent skyrmion size is reduced at −6 mm (approximately 100 nm, see the red profile).

Discussion

The contrast of magnetic Néel-type skyrmions in Fresnel defocus images of heavy metal/ferromagnet multilayers is often weak and can be obscured by strong diffraction contrast from the underlying polycrystalline grain structure of the sample. We have described a background subtraction procedure that can be used to improve the visibility of magnetic contrast recorded from skyrmions significantly. The approach involves setting the excitation

of the objective lens to an intermediate value that stabilizes individual magnetic skyrmions. The excitation of the objective lens is increased to saturate the sample and then decreased to the initial value. In this way, a sample that displays out-of-plane hysteresis can remain in a close-to-saturated state and the two Fresnel defocus images can be subtracted from each other to remove nonmagnetic contributions to the contrast. The rotation and magnification of the images are the same, making their alignment based on simple cross-correlation possible to compensate for any drift of the sample or the image. This approach works well if the change in excitation of the objective lens is relatively small (corresponding to a few tens of mT) between the acquisition of the skyrmion image and the background image. For larger variations, the hysteresis of the objective lens can affect the quality of the subtraction. The method can be used to remove undesirable variations in contrast due to crystal grains, supporting membrane and contaminants. The resulting improvement in magnetic contrast allows the use of smaller defocus values and provides an improvement in spatial resolution. It should be applicable to different multilayer samples with perpendicular anisotropy, although its degree of applicability will depend on the shape of the hysteresis curve. For the sample investigated here, the smallest defocus that could be used is approximately 400 μm (corresponding to a resolution of 30 nm) with a SNR of 1. In general, the best achievable resolution will depend on the strength of the magnetic field, the total thickness of the ferromagnetic layers, and diffraction contrast among other parameters. The stack observed here is quite thin as it contains only five repetitions. It can be expected that for thicker stacks (with for instance 10–15 repetitions), the magnetic signal would be stronger and then lower defocus could be used to improve the spatial resolution further.

Simulations show that delocalization effects in Fresnel defocus images can lead to inaccurate measurements of magnetic skyrmion size. Deviations can occur when the defocus is large enough that Fresnel fringes from opposite sides of a magnetic skyrmion overlap. As a result of such interference, the apparent magnetic skyrmion size does not follow a simple relationship with defocus. Three main situations can be distinguished, depending on the width of the Fresnel fringes compared to the true magnetic

skyrmion size. At small defocus values, i.e., when the width of the first Fresnel fringe w_f is smaller than the skyrmion radius ($w_f < d/2$), the apparent skyrmion size remains close to the true size. At intermediate defocus values, i.e., when w_f is between the radius and the diameter of the skyrmion ($d/2 < w_f < d$), the skyrmion size can be underestimated. At larger defocus values, i.e., when w_f exceeds the effective skyrmion diameter ($w_f > d$), the skyrmion size can be overestimated. These different possibilities can make it difficult to determine the true size of a small magnetic skyrmion that is not well resolved.

Conclusions

We have described a background subtraction procedure that can be used to improve the contrast of magnetic skyrmions in Fresnel defocus images of perpendicularly magnetized multilayers of heavy metals and ferromagnets. This approach reduces the influence of diffraction contrast from the crystal grains. It allows smaller defocus values to be used and provides an improvement in spatial resolution by a factor of approximately 3. Sub-mm defocus values could be used, while maintaining reasonable visibility, in order to study skyrmions that have sizes as small as 50 nm. This method should be beneficial for the interpretation of magnetic induction maps calculated using the transport-of-intensity equation (Teague, 1983; McCray et al., 2021). It is also equally applicable to in-focus magnetic imaging techniques, such as off-axis electron holography (see an example in Supplementary Information 6) (McCartney & Smith, 2007; Denneulin et al., 2021). Simulations show that the apparent size of a magnetic skyrmion recorded at a large defocus value can deviate significantly from its true size, emphasizing the need for strategies that allow image contrast to be optimized while improving spatial resolution, especially for the study of small magnetic skyrmions.

References

Benitez MJ, Hrabec A, Mihai AP, Moore TA, Burnell G, McGrouther D, Marrows CH & McVitie S (2015). Magnetic microscopy and topological stability of homochiral Néel domain walls in a Pt/Co/AlO$_x$ trilayer. *Nat Commun* **6**, 8957. https://dx.doi.org/10.1038/ncomms9957

Bernand-Mantel A, Camosi L, Wartelle A, Rougemaille N, Darques M & Ranno L (2018). The skyrmion-bubble transition in a ferromagnetic thin film. *SciPost Phys* **4**, 27. https://dx.doi.org/10.21468/SciPostPhys.4.5.027

Bogdanov AN & Rößler UK (2001). Chiral symmetry breaking in magnetic thin films and multilayers. *Phys Rev Lett* **87**, 037203. https://dx.doi.org/10.1103/PhysRevLett.87.037203

Boulle O, Vogel J, Yang H, Pizzini S, de Souza Chaves D, Locatelli A, Mentes TO, Sala A, Buda-Prejbeanu LD, Klein O, Belmeguenai M, Roussigné Y, Stashkevich A, Chérif SM, Aballe L, Foerster M, Chshiev M, Auffret S, Miron IM & Gaudin G (2016). Room-temperature chiral magnetic skyrmions in ultrathin magnetic nanostructures. *Nat Nanotechnol* **11**, 449. https://dx.doi.org/10.1038/nnano.2015.315

Braun HB (1994). Fluctuations and instabilities of ferromagnetic domain-wall pairs in an external magnetic field. *Phys Rev B* **50**, 16485–16500. https://dx.doi.org/10.1103/PhysRevB.50.16485

Büttner F, Lemesh I & Beach GSD (2018). Theory of isolated magnetic skyrmions: From fundamentals to room temperature applications. *Sci Rep* **8**, 4464. https://dx.doi.org/10.1038/s41598-018-22242-8

Caretta L, Mann M, Büttner F, Ueda K, Pfau B, Günther CM, Hessing P, Churikova A, Klose C, Schneider M, Engel D, Marcus C, Bono D, Bagschik K, Eisebitt S & Beach GSD (2018). Fast current-driven domain walls and small skyrmions in a compensated ferrimagnet. *Nat Nanotechnol* **13**, 1154–1160. https://dx.doi.org/10.1038/s41565-018-0255-3

Caron J (2018). Model-based reconstruction of magnetisation distributions in nanostructures from electron optical phase images. In *Key Technologies*, vol. 177. Jülich: Forschungszentrum Jülich GmbH Zentralbibliothek, Verlag.

Casiraghi A, Corte-León H, Vafaee M, Garcia-Sanchez F, Durin G, Pasquale M, Jakob G, Kläui M & Kazakova O (2019). Individual skyrmion manipulation by local magnetic field gradients. *Commun Phys* **2**, 145. https://dx.doi.org/10.1038/s42005-019-0242-5

Chapman JN (1984). The investigation of magnetic domain structures in thin foils by electron microscopy. *J Phys D: Appl Phys* **17**, 623–647. https://dx.doi.org/10.1088/0022-3727/17/4/003

Chen G, Ma T, N'Diaye AT, Kwon H, Won C, Wu Y & Schmid AK (2013). Tailoring the chirality of magnetic domain walls by interface engineering. *Nat Commun* **4**, 2671. https://dx.doi.org/10.1038/ncomms3671

Denneulin T, Caron J, Hoffmann M, Lin M, Tan HK, Kovács A, Blügel S & Dunin-Borkowski RE (2021). Off-axis electron holography of Néel-type skyrmions in multilayers of heavy metals and ferromagnets. *Ultramicroscopy* **220**, 113155. https://dx.doi.org/10.1016/j.ultramic.2020.113155

Dzyaloshinsky I (1958). A thermodynamic theory of weak ferromagnetism of antiferromagnetics. *J Phys Chem Solids* **4**, 241–255. https://doi.org/10.1016/0022-3697(58)90076-3

Fallon K, McVitie S, Legrand W, Ajejas F, Maccariello D, Collin S, Cros V & Reyren N (2019). Quantitative imaging of hybrid chiral spin textures in magnetic multilayer systems by Lorentz microscopy. *Phys Rev B* **100**, 214431. https://dx.doi.org/10.1103/PhysRevB.100.214431

Fert A, Reyren N & Cros V (2017). Magnetic skyrmions: Advances in physics and potential applications. *Nat Rev Mater* **2**, 17031. https://dx.doi.org/10.1038/natrevmats.2017.31

Garlow JA, Pollard SD, Beleggia M, Dutta T, Yang H & Zhu Y (2019). Quantification of mixed Bloch-Néel topological spin textures stabilized by the Dzyaloshinskii-Moriya interaction in Co/Pd multilayers. *Phys Rev Lett* **122**, 237201. https://dx.doi.org/10.1103/PhysRevLett.122.237201

He M, Li G, Zhu Z, Zhang Y, Peng L, Li R, Li J, Wei H, Zhao T, Zhang XG, Wang S, Lin SZ, Gu L, Yu G, Cai JW & Shen Bg (2018). Evolution of topological skyrmions across the spin reorientation transition in Pt/Co/Ta multilayers. *Phys Rev B* **97**, 174419. https://dx.doi.org/10.1103/PhysRevB.97.174419

He M, Peng L, Zhu Z, Li G, Cai J, Li J, Wei H, Gu L, Wang S, Zhao T, Shen B & Zhang Y (2017). Realization of zero-field skyrmions with high-density via electromagnetic manipulation in Pt/Co/Ta multilayers. *Appl Phys Lett* **111**, 202403. https://dx.doi.org/10.1063/1.5001322

Jadaun P, Register LF & Banerjee SK (2020). The microscopic origin of DMI in magnetic bilayers and prediction of giant DMI in new bilayers. *Npj Comput Mater* **6**, 88. https://dx.doi.org/10.1038/s41524-020-00351-1

Jiang W, Upadhyaya P, Zhang W, Yu G, Jungfleisch MB, Fradin FY, Pearson JE, Tserkovnyak Y, Wang KL, Heinonen O, te Velthuis SGE & Hoffmann A (2015). Blowing magnetic skyrmion bubbles. *Science* **349**, 283–286. https://dx.doi.org/10.1126/science.aaa1442

Jiang W, Zhang S, Wang X, Phatak C, Wang Q, Zhang W, Jungfleisch MB, Pearson JE, Liu Y, Zang J, Cheng X, Petford-Long A, Hoffmann A & te Velthuis SGE (2019). Quantifying chiral exchange interaction for Néel-type skyrmions via Lorentz transmission electron microscopy. *Phys Rev B* **99**, 104402. https://dx.doi.org/10.1103/PhysRevB.99.104402

Jiang W, Zhang X, Yu G, Zhang W, Wang X, Jungfleisch BM, Pearson J, Cheng X, Heinonen O, Wang KL, Zhou Y, Hoffmann A & te Velthuis SGE (2017). Direct observation of the skyrmion Hall effect. *Nat Phys* **13**, 162–169. https://dx.doi.org/10.1038/nphys3883

Kubetzka A, Pietzsch O, Bode M & Wiesendanger R (2003). Spin-polarized scanning tunneling microscopy study of 360° walls in an external magnetic

field. *Phys Rev B* **67**, 020401. https://dx.doi.org/10.1103/PhysRevB.67.020401

Li M, Lau D, De Graef M & Sokalski V (2019). Lorentz TEM investigation of chiral spin textures and Néel skyrmions in asymmetric [Pt/(Co/Ni)$_M$/Ir]$_N$ multi-layer thin films. *Phys Rev Mater* **3**, 064409. https://dx.doi.org/10.1103/PhysRevMaterials.3.064409

Li M, Rai A, Pokhrel A, Sapkota A, Mewes C, Mewes T, Graef MD & Sokalski V (2020). Formation of zero-field skyrmion arrays in asymmetric superlattices. *Appl Phys Lett* **117**, 112403. https://dx.doi.org/10.1063/5.0024265

Mansuripur M (1991). Computation of electron diffraction patterns in Lorentz electron microscopy of thin magnetic films. *J Appl Phys* **69**, 2455–2464. https://dx.doi.org/10.1063/1.348682

McCartney MR & Smith DJ (2007). Electron holography: Phase imaging with nanometer resolution. *Ann Rev Mater Res* **37**, 729–767. https://dx.doi.org/10.1146/annurev.matsci.37.052506.084219

McCray ARC, Cote T, Li Y, Petford-Long AK & Phatak C (2021). Understanding complex magnetic spin textures with simulation-assisted Lorentz transmission electron microscopy. *Phys Rev Appl* **15**, 044025. https://dx.doi.org/10.1103/PhysRevApplied.15.044025

McVitie S & Cushley M (2006). Quantitative Fresnel Lorentz microscopy and the transport of intensity equation. *Ultramicroscopy* **106**, 423–431. https://dx.doi.org/10.1016/j.ultramic.2005.12.001

McVitie S, Hughes S, Fallon K, McFadzean S, McGrouther D, Krajnak M, Legrand W, Maccariello D, Collin S, Garcia K, Reyren N, Cros V, Fert A, Zeissler K & Marrows CH (2018). A transmission electron microscope study of Néel skyrmion magnetic textures in multilayer thin film systems with large interfacial chiral interaction. *Sci Rep* **8**, 5703. https://dx.doi.org/10.1038/s41598-018-23799-0

Moreau-Luchaire C, Moutafis C, Reyren N, Sampaio J, Vaz CAF, Van Horne N, Bouzehouane K, Garcia K, Deranlot C, Warnicke P, Wohlhüter P, George JM, Weigand M, Raabe J, Cros V & Fert A (2016). Additive interfacial chiral interaction in multilayers for stabilization of small individual skyrmions at room temperature. *Nat Nanotechnol* **11**, 444. https://dx.doi.org/10.1038/nnano.2015.313

Moriya T (1960). Anisotropic superexchange interaction and weak ferromagnetism. *Phys Rev* **120**, 91–98. https://dx.doi.org/10.1103/PhysRev.120.91

Mühlbauer S, Binz B, Jonietz F, Pfleiderer C, Rosch A, Neubauer A, Georgii R & Böni P (2009). Skyrmion lattice in a chiral magnet. *Science* **323**, 915. https://dx.doi.org/10.1126/science.1166767

Nagaosa N & Tokura Y (2013). Topological properties and dynamics of magnetic skyrmions. *Nat Nanotechnol* **8**, 899. https://dx.doi.org/10.1038/nnano.2013.243

Nembach HT, Shaw JM, Weiler M, Jué E & Silva TJ (2015). Linear relation between Heisenberg exchange and interfacial Dzyaloshinskii–Moriya interaction in metal films. *Nat Phys* **11**, 829. https://dx.doi.org/10.1038/nphys3418

Park AM, Chen Z, Zhang XS, Zhu L, Muller DA & Fuchs GD (2020). Operando control of skyrmion density in a Lorentz transmission electron microscope with current pulses. *J Appl Phys* **128**, 233902. https://dx.doi.org/10.1063/5.0020373

Phatak C, Petford-Long AK & Graef MD (2016). Recent advances in Lorentz microscopy. *Curr Opin Solid State Mater Sci* **20**, 107–114. https://dx.doi.org/10.1016/j.cossms.2016.01.002

Pollard SD, Garlow JA, Yu J, Wang Z, Zhu Y & Yang H (2017). Observation of stable Néel skyrmions in cobalt/palladium multilayers with Lorentz transmission electron microscopy. *Nat Commun* **8**, 14761. https://dx.doi.org/10.1038/ncomms14761

Qin Z, Wang Y, Zhu S, Jin C, Fu J, Liu Q & Cao J (2018). Stabilization and reversal of skyrmion lattice in Ta/CoFeB/MgO multilayers. *ACS Appl Mater Interfaces* **10**, 36556–36563. https://dx.doi.org/10.1021/acsami.8b12694

Reimer L & Kohl H (2008). Wave optics of electrons. In *Transmission Electron Microscopy*, pp. 45–77, New York, NY: Springer New York. Available at https://link.springer.com/chapter/10.1007/978-0-387-40093-8_1

Romming N, Kubetzka A, Hanneken C, von Bergmann K & Wiesendanger R (2015). Field-dependent size and shape of single magnetic skyrmions. *Phys Rev Lett* **114**, 177203. https://dx.doi.org/10.1103/PhysRevLett.114.177203

Schott M, Bernand-Mantel A, Ranno L, Pizzini S, Vogel J, Béa H, Baraduc C, Auffret S, Gaudin G & Givord D (2017). The skyrmion switch: Turning magnetic skyrmion bubbles on and off with an electric field. *Nano Lett* **17**, 3006–3012. https://dx.doi.org/10.1021/acs.nanolett.7b00328

Soumyanarayanan A, Raju M, Gonzalez Oyarce AL, Tan AKC, Im MY, Petrovic A, Ho P, Khoo KH, Tran M, Gan CK, Ernult F & Panagopoulos C (2017). Tunable room-temperature magnetic skyrmions in Ir/Fe/Co/Pt multilayers. *Nat Mater* **16**, 898. https://dx.doi.org/10.1038/nmat4934

Teague MR (1983). Deterministic phase retrieval: A Green's function solution. *J Opt Soc Am* **73**, 1434–1441. https://dx.doi.org/10.1364/JOSA.73.001434

Woo S, Litzius K, Krüger B, Im MY, Caretta L, Richter K, Mann M, Krone A, Reeve RM, Weigand M, Agrawal P, Lemesh I, Mawass MA, Fischer P, Kläui M & Beach GSD (2016). Observation of room-temperature magnetic skyrmions and their current-driven dynamics in ultrathin metallic ferromagnets. *Nat Mater* **15**, 501. https://dx.doi.org/10.1038/nmat4593

Yang H, Thiaville A, Rohart S, Fert A & Chshiev M (2015). Anatomy of Dzyaloshinskii-Moriya interaction at Co/Pt interfaces. *Phys Rev Lett* **115**, 267210. https://dx.doi.org/10.1103/PhysRevLett.115.267210

Yu XZ, Onose Y, Kanazawa N, Park JH, Han JH, Matsui Y, Nagaosa N & Tokura Y (2010). Real-space observation of a two-dimensional skyrmion crystal. *Nature* **465**, 901. https://doi.org/10.1038/nature09124

Zhang S, Zhang J, Wen Y, Chudnovsky EM & Zhang X (2018a). Creation of a thermally assisted skyrmion lattice in Pt/Co/Ta multilayer films. *Appl Phys Lett* **113**, 192403. https://dx.doi.org/10.1063/1.5053983

Zhang S, Zhang J, Wen Y, Chudnovsky EM & Zhang X (2018b). Determination of chirality and density control of Néel-type skyrmions with in-plane magnetic field. *Commun Phys* **1**, 36. https://dx.doi.org/10.1038/s42005-018-0040-5

Zhang S, Zhang J, Wen Y, Peng Y, Qiu Z, Matsumoto T & Zhang X (2020). Deformation of Néel-type skyrmions revealed by Lorentz transmission electron microscopy. *Appl Phys Lett* **116**, 142402. https://dx.doi.org/10.1063/5.0002592

Zhang S, Zhang J, Zhang Q, Barton C, Neu V, Zhao Y, Hou Z, Wen Y, Gong C, Kazakova O, Wang W, Peng Y, Garanin DA, Chudnovsky EM & Zhang X (2018c). Direct writing of room temperature and zero field skyrmion lattices by a scanning local magnetic field. *Appl Phys Lett* **112**, 132405. https://dx.doi.org/10.1063/1.5021172

Appendix A. Analytical Expression for Skyrmion Magnetization

To obtain the magnetization distribution of an individual magnetic skyrmion with well-defined dimensions, we used standard analytical expressions that approximate it as a 360° magnetic domain wall (Braun, 1994; Romming et al., 2015). The magnetization **M** is defined in a cylindrical coordinate system $\mathbf{M} = (M_r, M_\varphi, M_z)$ as

$$\mathbf{M} = [\,\cos(\phi)\sin(\theta(r)),\ \sin(\phi)\sin(\theta(r)),\ \cos(\theta(r))], \qquad (A.1)$$

where $\phi = 0$ for a Néel-type magnetic domain wall and

$$\theta(r) = \pi + \arcsin\left[\tanh\left(\frac{r - d/2}{w}\right)\right] + \arcsin\left[\tanh\left(\frac{r + d/2}{w}\right)\right], \qquad (A.2)$$

where d is the magnetic skyrmion diameter and w is the magnetic domain wall width parameter. In Figure 5, the magnetic domain wall width parameter was set to $w = 19/\pi$ nm based on an experimental measurement carried out using off-axis electron holography (see Supplementary Information 6).

Appendix B. Simulation of Fresnel Defocus Images

Magnetization distributions obtained using analytical expressions described in the previous section were used as an input to an optimized forward model programmed in Python for simulating magnetic-phase images (Caron, 2018). First, the two-dimensional magnetization distributions were extended to create three-dimensional distributions, taking into account the thicknesses of the ferromagnetic layers. In Figure 5, the magnetization distribution was set as purely Néel-type and invariant through the specimen thickness. (Additional simulations for mixed Bloch-Néel skyrmions are shown in Supplementary Information 7.) Second, the three-dimensional magnetization distribution was projected onto a two-dimensional, two-component vector field $\mathbf{M}_{proj}(x, y) = (M_{proj,x}(x, y);\ M_{proj,y}(x, y))$, taking into account the tilt of the

specimen with respect to the incident electron beam direction. The magnetostatic contribution to the phase can then be written in the form (Mansuripur, 1991)

$$\varphi_{\mathrm{mag}}(x, y) = -\frac{\mu_0}{2\Phi_0} \int \frac{(y - y')M_{\mathrm{proj,x}}(x', y') - (x - x')M_{\mathrm{proj,y}}(x', y')}{(x - x')^2 + (y - y')^2} \, dx' \, dy',$$

(B.1)

where μ_0 is the vacuum permeability and $\Phi_0 = \pi\hbar/e$ is the magnetic flux quantum. The third step of the simulation approximates every pixel in the discretized projected distribution using simple homogeneously magnetized geometries such as discs or squares, which have known phase contributions, in order to calculate the final magnetic phase image. The discretization is carried out in real space, while the subsequent convolution of the two projected magnetization components with the respective kernels for simple geometries is carried out in Fourier space.

Fresnel defocus images were then calculated from the phase images by setting up a wave function of the form $\Psi(x, y) = e^{i\varphi_{\mathrm{mag}}(x,y)}$, which was multiplied in Fourier space by a phase plate according to the expression

$$\Psi_{\mathrm{LTEM}}(x, y) = \mathcal{F}_2^{-1}\{\mathcal{F}_2\{e^{i\varphi_{\mathrm{mag}}(x,y)}\} \cdot e^{-i\chi(q_x,q_y)}\},$$

(B.2)

where $\mathcal{F}_2\{\ldots\}$ and $\mathcal{F}_2^{-1}\{\ldots\}$ denote a two-dimensional Fourier transform and its inverse, while $\chi(q_x, q_y)$ denotes an aberration function, which takes the form (Chapman, 1984)

$$\chi(q_x, q_y) = \pi\lambda\Delta f(q_x^2 + q_y^2)$$

(B.3)

and only contains the term for defocus Δf in this work. The spherical aberration of the Lorentz lens and divergence of the electron source (damping envelope) were not taken into account here, but their influence on simulated Fresnel images is discussed in Supplementary Information 8.

The intensity of the final Fresnel defocus images is then given by the expression

$$I_{\mathrm{LTEM}}(x, y) = \Psi_{\mathrm{LTEM}}(x, y) \cdot \Psi_{\mathrm{LTEM}}^*(x, y).$$

(B.4)

Input parameters for the simulations are defocus, sample tilt angle, the total thickness of the ferromagnetic layers, and the saturation magnetization. In Figure 5, the defocus was varied and the other parameters were, respectively, 20°, 6 nm (based on calibrated deposition rates), and 0.92 T (based on bulk magnetic measurements).